Influence of the imaginary component of the photonic potential on the properties of solitons in $\mathcal{PT}$-symmetric systems

Chandroth P. Jisha,[1,*] Lini Devassy,[2] Alessandro Alberucci,[3] and V. C. Kuriakose[2]

[1]*Centro de Física do Porto, Faculdade de Ciências, Universidade do Porto, R. Campo Alegre 687, Porto 4169-007, Portugal*

[2]*Department of Physics, Cochin University of Science and Technology, Cochin 682022, India*

[3]*Nonlinear Optics and Optoelectronics Laboratory, University "Roma Tre", Via della Vasca Navale 84, 00146 Rome, Italy*

(Received 16 June 2014; published 27 October 2014)

Existence, stability, and dynamics of $\mathcal{PT}$-symmetric fundamental bright solitons supported by localized super-Gaussian potentials in a focusing Kerr medium are investigated theoretically. We address how the shape and the magnitude of the transverse profile of the loss-gain distribution affect soliton stability. We find the stability region for nonlinear wave packets via a linear stability analysis, interpreting the insurgence of instability as an unbalanced flow of energy on the transverse plane. We confirm our results via numerical simulations, showing that an unstable soliton first undergoes longitudinal oscillations in propagation due to the interference between the soliton and the exponentially growing perturbation modes, eventually forming a highly localized single peak in the gain region.

DOI: 10.1103/PhysRevA.90.043855 PACS number(s): 42.65.Tg, 03.65.Ge, 11.30.Er, 42.70.Qs

I. INTRODUCTION

The postulates of quantum mechanics assume the Hermiticity of any operator associated with any measurable quantity, the latter defined as an observable. Bender and Boettcher [1] generalized this axiom in a complex domain [2] by showing that a certain class of complex non-Hermitian Hamiltonians can have real spectra if they obey parity time ($\mathcal{PT}$) symmetry. The parity reflection operator $\mathcal{P}$ and time-reversal operator $\mathcal{T}$ are defined by their action on the position and momentum operators $\hat{x}$ and $\hat{p}$ as $\hat{p} \to -\hat{p}$, $\hat{x} \to -\hat{x}$ and $\hat{p} \to -\hat{p}$, $\hat{x} \to \hat{x}$, $i \to -i$, respectively; from the above conditions, it can be shown that the potentials associated with non-Hermitian Hamiltonians must satisfy $V(\hat{x}) = V^*(-\hat{x})$ [3]. This concept of $\mathcal{PT}$ symmetry of a non-Hermitian Hamiltonian generalizes quantum mechanics in a complex domain [2,4]. Even though inadequacy of $\mathcal{PT}$ symmetry to model fundamental laws of physics has been recently pointed out [5], its applications in various areas of physics remain important and fruitful, ranging from $\mathcal{PT}$-symmetric quantum oscillators [1] to linear [6,7] and nonlinear optics [8,9], from electronics [10] to quantum field theory [11]. The most fertile field has certainly been optics, where the $\mathcal{PT}$-symmetry condition reads $n(x) = n^*(-x)$, where $n(x)$ is the pointwise dependent complex refractive index of the material [12,13]: such transverse photonic potential can be realized in optics, leading to experimental demonstration of $\mathcal{PT}$-symmetric systems in AlGaAs [14], photorefractive materials [6], silicon [15,16], fiber optics [17], and light-written guides in glass [18]. Several exotic effects have been predicted, such as unidirectional light propagation in complex Bragg grating [19], double refraction and power oscillations [20], nonreciprocal Bloch oscillations [21], the perfect coherent absorber [22], and multistability [23].

The enormous interest about $\mathcal{PT}$ symmetry in optics led soon to its generalization to the nonlinear case, the latter providing several interesting predictions, most of them still waiting for an experimental verification; very recently, nonlinear enhancement in the broken $\mathcal{PT}$ case and nonreciprocal propagation has been observed in a pair of coupled ring resonators [24]. The action of Kerr nonlinearity in $\mathcal{PT}$-symmetric systems with localized and periodic photonic potentials was analyzed first in Ref. [8] with reference to optical bright solitons, that is, electromagnetic waves preserving their shape in propagation due to the self-focusing effect [25]. Dependence on optical power of the complex band structure, comprising the $\mathcal{PT}$ transition, has been formulated both for solitons [8] and nonlinear Bloch waves [9]. Following works studied existence and stability of solitons both in periodic and in localized $\mathcal{PT}$ potentials. Gap solitons have been discussed both in focusing and defocusing materials [26,27], including dependence on nonlocality [28,29]; existence of solitons in the presence of a linear defect in a periodic potential has been discussed as well [30]. Light self-trapping has been investigated also in directional couplers [31]. Regarding localized photonic potentials, fundamental and higher-order solitons supported by complex $\mathcal{PT}$-symmetric Gaussian potentials have been studied for a focusing [32] and a defocusing [33] local Kerr nonlinearity.

In the present work, we analyze existence and stability of $\mathcal{PT}$-symmetric solitons supported by Gaussian and super-Gaussian defects in a material encompassing local Kerr focusing nonlinearity, addressing how the transverse profile of the imaginary potential affects light self-localization: specifically, the behavior of the exceptional points and soliton stability via a linear perturbation analysis is investigated. To understand how the imaginary part of the photonic potential affects nonlinear waves is a fundamental issue, both in view of possible applications (e.g., active optical cavities) as well as for the basic physics (i.e., understanding how the energy transverse flux affects the self-localization of nonlinear waves). We describe how wave instability develops: specifically, we demonstrate that the wave does not undergo a simple exponential amplification, but it is subjected to an oscillatory motion due to the interference between the solitonic wave and the perturbation mode, eventually leading to the appearance of a strongly peaked spike in correspondence to the peak region. To reach this goal, two different transverse

*Corresponding author: cpjisha@gmail.com

profiles for the loss-gain distribution are examined. The dependence of stability on the propagation constant (energy for matter waves) is analyzed via a standard linear analysis, showing that fundamental bright solitons below the linear $\mathcal{PT}$-symmetry breaking point undergo negligible (with respect to their own Rayleigh distances) exponential amplification, whereas fundamental bright solitons are affected by strong instabilities when the underlying linear system spontaneously breaks the $\mathcal{PT}$ symmetry. Predictions stemming from the linear analysis are confirmed via beam propagation method (BPM) simulations. Additionally, BPM simulations allow us to study beam dynamics even beyond the perturbative limit assumed by linear stability analysis: we show that the exponential instability is accompanied by an oscillation in the soliton trajectory due to the coherent interaction between the soliton and the dominant unstable mode; when the instability mode starts to dominate, a sharp peak in the gain region is observed, subjected to an exponential growth enhanced by the self-focusing effect. We would also like to stress that, according to the available literature [20,32], solitons should be stable below the exceptional point: we demonstrate that this statement is wrong, showing that solitons actually are quasistable; that is, the distance necessary for the instability to become appreciable is much longer than the Rayleigh distance of the soliton.

II. DEFINITION OF THE PHYSICAL SYSTEM

Propagation of monochromatic light in a (1+1)-dimensional local Kerr medium embedding a linear defect obeys a modified nonlinear Schrödinger equation (NLSE) [34]:

$$i\frac{\partial E}{\partial z} = -\frac{1}{2k}\frac{\partial^2 E}{\partial x^2} - k_0 n_2 |E|^2 E - k_0 \Delta n(x) E, \qquad (1)$$

where k_0 is the vacuum wave number, $k = n_0 k_0$ with n_0 the unperturbed refractive index of the medium, E is the electric field, n_2 is the Kerr coefficient, x is the transverse coordinate, z is the propagation direction, and $k_0\Delta n(x) = k_0\Delta n_R(x) + ik_0\Delta n_I(x)$ is the linear local variation in the refractive index distribution, the real part $\Delta n_R(x)$ and the imaginary part $\Delta n_I(x)$ representing the local phase delay and the gain or loss distribution, respectively. Hereafter we will refer to focusing nonlinearity, that is, $n_2 > 0$. Defining w_p as the typical width of the linear refractive index profile Δn and the normalized longitudinal length $L_p = n_0 k_0 w_p^2$, Eq. (1) can be normalized defining $\xi = x/w_p$, $\zeta = z/L_p$, and $\psi = \sqrt{n_0 n_2 w_p^2 k_0^2}\,E$, providing [35]

$$i\frac{\partial \psi}{\partial \zeta} = -\frac{1}{2}\frac{\partial^2 \psi}{\partial \xi^2} - |\psi|^2\psi + V(\xi)\psi, \qquad (2)$$

where we defined the effective potential $V(x) = -n_0 k_0^2 w_p^2 \Delta n(x)$. The Rayleigh length, $L_{R_x} = k w_x^2/2$, in the normalized framework becomes $L_{R_\xi} = w_\xi^2/2$, where w_x and w_ξ are the waist of the beam in physical and normalized coordinates, respectively. We stress that Eq. (2) governs evolution of the Bose-Einstein condensate (BEC) as well [36].

In case of a $\mathcal{PT}$-symmetric potential, the potential satisfies the condition $V_R(\xi) = V_R(-\xi)$ and $V_I(\xi) = -V_I(-\xi)$. In this paper we will consider a super-Gaussian for the real part of the potential:

$$V_R(\xi) = -V_r \exp(-\xi^{2l}). \qquad (3)$$

Thus, $l = 1$ means a Gaussian profile, whereas for large l the potential V_R tends to a rectangular distribution. This choice allows us to consider all the possible types of confining structures presenting a single guiding layer, ranging from step-index to smooth guides.

For the imaginary part we will consider two different profiles in order to understand how transverse motion of photons induced by inhomogeneous gain or loss affects light propagation. Specifically, in the first case (called hereafter type A) we will take V_I equal to the first derivative of V_R, thus providing

$$V_I^A(\xi) = V_i \xi^{2l-1} \exp(-\xi^{2l}). \qquad (4)$$

When l increases, the loss or gain region becomes increasingly concentrated at the edges of the potential, the two peaks getting narrower as well. Thus, changing l it is possible to verify how the spatial overlap between the self-confined wave and the gain or loss region affects field evolution. We will consider also the following class of potential, hereafter named type B:

$$V_I^B(\xi) = V_i \xi \exp(-\xi^{2l}). \qquad (5)$$

Profiles of V_I almost maintain their shape as l changes, i.e., when the real potential $V_R(\xi)$ is varied; in other words, the gain or loss distribution is not subject to spatial localization on the edge of the real potential when parameter l grows up. Thus, type B potentials will be employed to address the dependence of the field evolution on the transverse distribution of the linear refractive index.

III. STATIONARY SOLUTIONS IN THE LINEAR CASE

Before dealing with the nonlinear case, let us study the existence and the behavior of confined modes in the linear case, i.e., in the absence of the Kerr effect. Bound states can be found numerically from Eq. (2) making the ansatz $\psi(\xi,\zeta) = \phi(\xi)e^{i\mu\zeta}$, providing the linear eigenvalue problem $\mu\phi = \frac{1}{2}\frac{\partial^2\phi}{\partial\xi^2} - (V_R + iV_I)\phi$. Noteworthy, due to the presence of dissipative terms, eigenvalue μ in general will be complex; that is, we can write $\mu = \mu_R + i\mu_I$. Hereafter we will refer to the fundamental guided mode (in quantum mechanics commonly called the ground state), i.e., we will consider the eigenfunctions with the highest μ_R. Throughout the text, we have fixed $V_r = 1$. Figures 1 and 2 show that eigenvalues of the system follow an analogous behavior as the gain or loss magnitude V_i is changed. In fact, for V_i lower than a critical value V_c, $\mathcal{PT}$ symmetry is conserved and all the eigenvalues are real; in particular the maximum μ_R, the latter corresponding to two degenerate eigenmodes, is positive, in accordance with the well-known Hermitian case, i.e., for vanishing V_i. The eigenmode has a symmetric real and antisymmetric imaginary part (see Fig. 1, last row, last column). Condition $V_i = V_c$ identifies the exceptional point where $\mathcal{PT}$ symmetry is spontaneously broken: the two eigenvalues corresponding to the maximum μ_R becomes complex; thus the corresponding eigenmodes are subjected to an exponential decay or amplification, according to the sign of

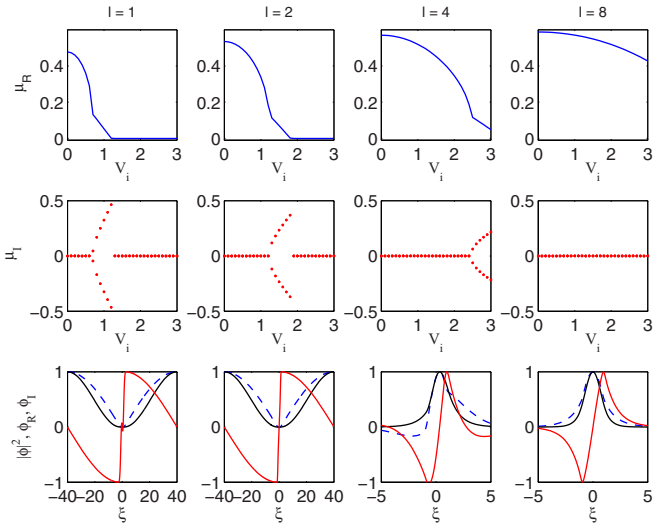

FIG. 1. (Color online) Ground state μ vs V_i for the linear potential of type A. The top row depicts real part μ_R and the middle row depicts imaginary part μ_I, plotted vs V_i. Imaginary eigenvalues with equal magnitude but opposite in sign appear at the exceptional point. The stationary profile at $V_i = 3$, which falls in a different spectral region for each l, is plotted in the last row; the black symmetric solid line is the intensity, the blue dashed line is the real part of ϕ, and finally the antisymmetric red solid line is the imaginary part of the field ϕ. Here $V_r = 1$.

the imaginary part of μ. The real part of the eigenmode now becomes asymmetric (an example is shown in Fig. 1, last row, third column). Further increases in V_i induce an almost linear growth for $|\mu_I|$; μ_R follows a falling quasilinear trend versus V_i as well. This trend is abruptly interrupted for a certain threshold V_t: afterward, both the μ_R and μ_I vanish. At this point eigenvalues are in the continuum and the corresponding

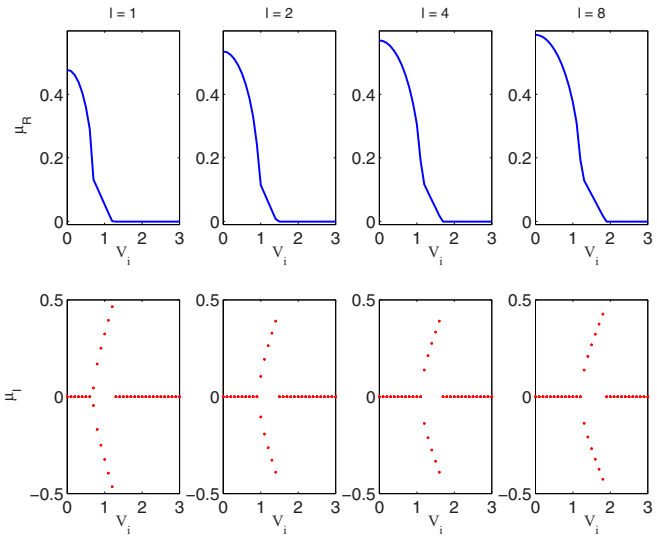

FIG. 2. (Color online) Ground state μ vs V_i for the linear potential of type B. The top row depicts real part μ_R and the bottom row depicts imaginary part μ_I, plotted vs V_i. As compared to type A, the trend of the eigenvalue μ_I vs V_i depends much less on l given that $V_I(\xi)$ is kept constant. Here $V_r = 1$.

eigenmodes are spread in space (see Fig. 1, last row, first two columns; the size of the numerical grid is $[-40\ 40]$ with solutions required to vanish at the boundary).

The dynamics described above is shared by both the types of imaginary potentials V_I described by Eqs. (4) and (5). For potentials of type A [Eq. (4)] the critical potential is $V_c^A \approx lV_r/2 + 1/5$ (i.e., it linearly increases with l) and follows more or less the trend for analytically solvable complex Scarf II potential [37], whereas for the type B [Eq. (5)] the transition occurs at $V_c^B \geqslant V_r$ for $l \geqslant 2$ ($l = 1$ is analogous to type A), precisely undergoing small increases as l gets larger. The threshold potential V_t follows an analogous trend, the increase with V_i being larger for potentials of type A.

The behavior of V_c and V_t with the shape of $V_I(\xi)$ can be understood invoking the conservation of photons on each point of the transverse plane [8,29]. Let us define the transverse component of the Poynting vector as $j = \frac{1}{2i}(\psi^* \frac{\partial \psi}{\partial \xi} - \psi \frac{\partial \psi^*}{\partial \xi})$ and the local intensity as $\rho = |\psi|^2$. For stationary modes we have $\partial\rho/\partial\zeta = 0$; then conservation of photons provides [29]

$$\frac{\partial}{\partial \xi}\left(\rho \frac{\partial \chi}{\partial \xi}\right) = 2V_i(\xi)\rho, \tag{6}$$

where $\phi = \sqrt{\rho}e^{i\chi(\xi)}$. Equation (6) tells us that the eigenmodes acquire a nonvanishing transverse profile, in turn inducing a net motion of photons from the gain to loss regions, as required to conserve local intensity during evolution along ζ. In particular, large potentials V_i imply a nonsustainable transverse flux of particles, leading to a continuous increase of the energy in correspondence to the gain regions; mathematically, what happens is that Eq. (6) does not have any solution, corresponding to an intensity ρ varying exponentially along ζ. Our results confirm this interpretation: For potentials of type A, the overlap between the mode and V_I decreases as l gets larger, thus explaining the behavior of V_c^A with l. For the same reason, $\mathcal{PT}$ symmetry is broken at lower V_i for potentials of type B than for type A.

IV. STATIONARY SOLUTIONS IN THE NONLINEAR CASE

Let us now discuss the nonlinear case. In full analogy with the linear case, solitonic solutions of Eq. (2) are in the form $\psi(\xi,\zeta) = \phi(\xi)\exp(i\mu\zeta)$, μ being the propagation constant (the chemical potential in the BEC case); noteworthy, due to the Kerr effect both $\phi(\xi)$ and μ depend on the power carried by the wave, defined in our dimensionless framework as $P = \int |\psi|^2 d\xi$. Equation (2) turns into

$$\mu\phi = \frac{1}{2}\frac{\partial^2\phi}{\partial\xi^2} - (V_R + iV_I)\phi + |\phi|^2\phi. \tag{7}$$

Stationary solutions of Eq. (7) are sought using standard relaxation technique based on pseudospectral differentiation with Fourier differentiation matrices [38]. We look for stationary solutions for different l and V_I keeping the amplitude of real part V_r fixed and equal to 1. Typical profiles of the shape-invariant solutions for potentials of type A are depicted in Fig. 3 and for potentials of type B in Fig. 4; noteworthy, in both figures soliton transverse profiles for fixed values of the eigenvalue μ are plotted. In accordance with Eq. (6), fundamental solitons have an even real part

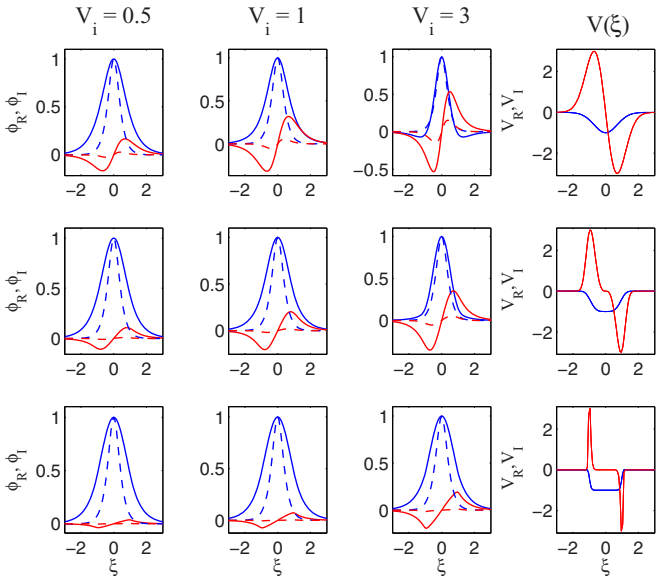

FIG. 3. (Color online) Soliton profiles for potentials of type A for $l = 1$, 2, and 8 (top to bottom rows) for V_i as marked. Symmetric solid curves represent the normalized real part of the profile for $\mu = 1.3$ (solid lines) and $\mu = 6$ (dashed lines). Antisymmetric curves represent the imaginary part normalized to the peak of the real part; the higher the magnitude the lower the μ. The behaviors of V_R (blue symmetric lines) and V_I (red antisymmetric lines) vs ξ are shown in the last column for each l for $V_i = 3$.

and an odd imaginary part [8,29,32,33]. The most striking effect ascribable to the nonlinearity is the *generation* of a nonlinear bound state featuring $\mu_R > 0$ and $\mu_I = 0$, regardless of the magnitude of V_i (i.e., even above the exceptional point): differently stated, the nonlinearity provokes a transition from broken $\mathcal{PT}$ to a $\mathcal{PT}$-symmetric state [8,9,29], even if all the linear eigenvalues are complex.

Let us now discuss the soliton properties depending on the shape of the potential, starting from type A. For $V_i = 0.5$ soliton profiles are slightly perturbed by the small transverse flux [see Eq. (6)], whatever the power and the degree l are.

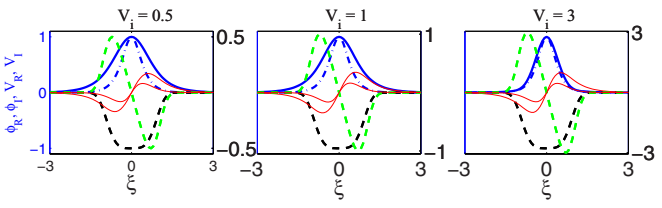

FIG. 4. (Color online) Soliton profiles for potentials of type B for $l = 2$ (other values of l provide almost identical results), for V_i as marked. Symmetric blue curves represent the normalized real part of the profile for $\mu = 1.8$ (solid lines) and $\mu = 6$ (dash-dotted lines). Solid red lines are the imaginary component of the field normalized with respect to the peak of the real part: the higher the magnitude the lower the μ. Symmetric dashed black lines represent the real part of the potential. The antisymmetric dashed green line represents the imaginary part of the potential. Symmetric curves correspond to the left axis and antisymmetric curves correspond to the right axis, respectively.

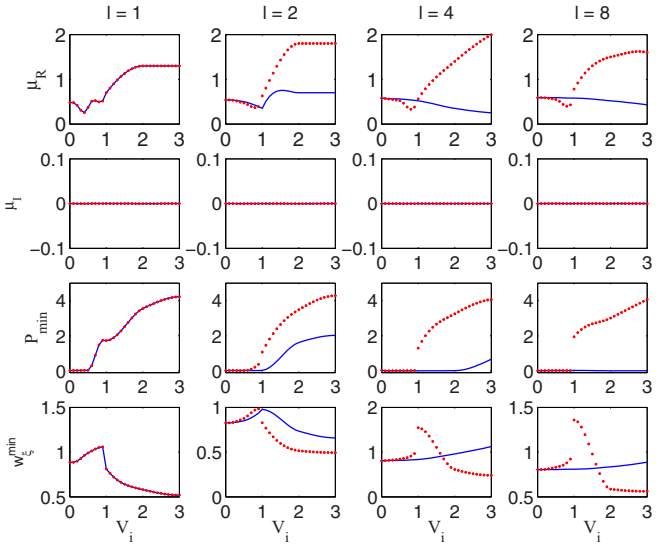

FIG. 5. (Color online) Features of the fundamental soliton vs V_i for the lowest μ_R allowed, for potentials of both type A (blue solid lines) and type B (red points). The first two rows depict real part μ_R and imaginary part μ_I, respectively. The corresponding minimum power $P_{\min}$ and width $w_\xi^{\min}$ of the soliton are plotted in the last two rows.

Increasing the magnitude of V_i, profiles of ϕ are affected by the dissipative terms when power is small, corresponding to wide solitons strongly overlapping with the gain or loss regions. To minimize the spatial overlap between the intensity distribution and the gain or loss regions, solitons get narrower as V_i increases [see the third column in Fig. 3]. In agreement with this interpretation, this effect disappears as l is increased. Solitons propagating in type B potentials confirm our interpretation. In fact, regardless of the shape of V_R (i.e., independently from l), solitons get narrower as V_i is raised up, given that the spatial shape of V_I does not vary appreciably with l.

An overview of the features of the fundamental soliton showing the minimum μ_R for fixed V_i and l is reported in Fig. 5. Noticeably, there is no upper cutoff in the value of either μ or V_i at which nonlinear shape-preserving solutions cease to exist. Conversely, the minimum value of μ_R does not correspond with the linear value (i.e., for small P) when a significant spatial overlap between the soliton and V_i exists, as shown in Fig. 5. The net effect is the generation of a minimum power for the soliton formation, a peculiarity of $\mathcal{PT}$-symmetric systems, not occurring in transparent bulk media showing a focusing response and a trapping linear potential [8,39]. Confirming our physical interpretation, for potentials belonging to type A the case $l = 1$ corresponds to the largest growth of the minimum power $P_{\min}$ versus V_I, the curve flattening toward the linear value $P_{\min} = 0$ for large l (see the solid lines in the third row in Fig. 5); on the other hand, for potentials of type B the trend of $P_{\min}$ versus V_I depends weakly on l, given that the imaginary potential V_i stays unvaried (see the marks in the third row in Fig. 5). The corresponding soliton width $w_\xi^{\min}$ behaves according to our interpretation: when $P_{\min}$ diverges from zero, the soliton becomes narrower than the corresponding linear eigenmode (the fourth row in Fig. 5).

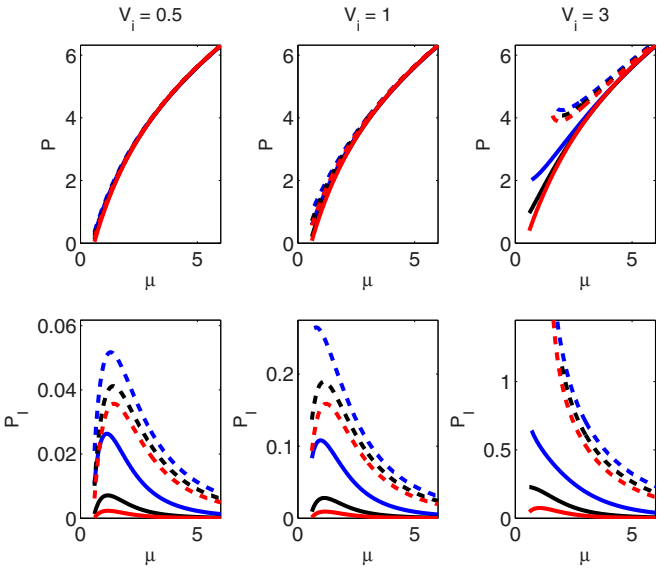

FIG. 6. (Color online) Total power P (top) and the corresponding power carried in the imaginary component P_I (bottom) for potentials of type A (solid lines) and of type B (dashed lines) for $l = 2$ (blue), 4 (black), and 8 (red), from top to bottom curves, respectively; V_i values are marked in the figure. For low V_i total power P follows the same trend for both the potentials.

We stress that, as we will show in the following section, solitons obtained for V_i values above the $\mathcal{PT}$-symmetry breaking point tend to be strongly unstable. This is in contrast to the periodic case where the nonlinear Bloch waves found at the exceptional point were shown to be stable with respect to $\mathcal{PT}$-breaking perturbations, even if undergoing a small modulation instability due to the nonlinear dynamics [9].

Finally, we address the relative weight of the real and the imaginary part of $\phi(\xi)$, labeled with ϕ_R and ϕ_I, respectively. The overall power can be written as $P = P_R + P_I = \int |\phi_R|^2 d\xi + \int |\phi_I|^2 d\xi$ to enlighten the two different contributions. Behavior of power P versus μ_R for different V_i and l is plotted in Fig. 6. The two trends for potentials of type A and of type B tend to converge to the same curve for large powers, the curve being independent both from l and V_i; the soliton width undergoes an analogous trend. Physical explanation is straightforward: the nonlinear refractive index becomes dominant, and the effect of the linear potential $V(\xi)$ becomes negligible. At low powers a different behavior occurs: first, existence curves in the plane (μ, P) change both with l and V_i; moreover, when V_i is high and l is low, soliton existence curves for the two types of potentials diverge at small powers. In particular, differently from solitons in non-dissipative confining potentials [34], a power threshold for soliton existence appears (the effect is maximum for the curve at $V_i = 3$) given that the nonlinear index well needs to be large enough to compensate the transverse flux. The power in the imaginary part P_I versus μ decreases owing to the larger light confinement around $\xi = 0$, at the same time increasing with V_i. Noticeably, the magnitude of power in the imaginary component is larger for potential B than potential A due to the larger overlap with the dissipative regions. In short, $\mathcal{PT}$-symmetric systems exhibit a power threshold; i.e., there is a minimum cutoff for soliton existence which increases with increasing V_i (Fig. 5). Previous works on localized potentials [20] have only dealt with this important topic marginally and have not discussed in detail how the soliton minimum power depends on the linear potential.

V. LINEAR STABILITY ANALYSIS

In order to understand the dynamical behavior, we now address the stability analysis of the stationary solutions with respect to small perturbations. The stability of the solution is analyzed by considering perturbations to the solitonic solutions in the form $\psi = [\phi + a(\xi,\zeta)]\exp(i\mu\zeta)$ with $a(\xi,\zeta) = p(\xi)\exp(i\lambda\zeta) + q(\xi)\exp(-i\lambda^*\zeta)$, yielding the linearized eigenvalue problem [8]:

$$\lambda \begin{bmatrix} p \\ q^* \end{bmatrix} = \begin{bmatrix} L_1 - iV_I(\xi) & \phi^2 \\ -(\phi^*)^2 & -L_1 - iV_I(\xi) \end{bmatrix} \begin{bmatrix} p \\ q^* \end{bmatrix}, \quad (8)$$

where $L_1 = -\mu + \frac{1}{2}\frac{\partial^2}{\partial x^2} + 2|\phi|^2 - V_R$. The solution is linearly stable if $\mathrm{Im}(\lambda) = 0$ for every λ, i.e., if the system possesses solely real eigenvalues. Owing to the $\mathcal{PT}$-symmetric nature of the system, the eigenvalues appear in complex conjugate pairs (i.e., if λ is an eigenvalue, λ^* is an eigenvalue as well). According to the global features of all the λ stemming from Eq. (8), in general the wave behavior can be grouped into three main categories. If all the eigenvalues are purely real, nonlinear wave propagation is linearly stable; if at least one of the eigenvalues is purely imaginary, soliton shape is destroyed in evolution due to exponential amplification of noise; finally, if eigenvalues are complex, oscillatory instability is observed. Oscillatory instability (OI) with $\mathrm{Im}(\lambda) > 0 (<0)$ implies exponentially decaying (growing) modes, combined with a longitudinal periodic variation of the intensity profile [34].

We found numerically that all the eigenvalues computed from Eq. (8) are either real or complex; thus nonlinear wave evolution can be either linearly stable or subjected to OI; moreover, eigenvalues appear in quartets (including λ, λ^*, $-\lambda$, and $-\lambda^*$; check [29,40] and references therein). As an example, the profiles of the eigenmodes corresponding to the maximum growth rate (fixed by λ_{dom}) are shown in Fig. 7, for four different values of V_i and having set $l = 1$ and $\mu = 1.3$. Two different regimes can be identified: a quasilinearly stable (that is, an amplification length of the instability mode much larger than the Rayleigh distance) region for low V_i corresponding to unbroken $\mathcal{PT}$ symmetry in the linear case (case $V_i = 0.1$ and 0.5 in Fig. 7; compare with the linear spectrum plotted in Fig. 1) and OI for high V_i (case $V_i = 0.9$ and 1, corresponding to broken $\mathcal{PT}$ symmetry in the linear regime). As expected, in the case of the regime of high instability the modes associated with quartets of eigenvalues are featured by a strongly asymmetric profile with respect to the transverse coordinate ξ, corresponding to growing or decaying modes, if the field is concentrated into the gain or loss region, respectively.

The correspondence between soliton stability and the linear spectrum of the system holds valid, regardless of the values assumed by μ and l and of the type of potential (A or B). Figure 8 summarizes this property: here the imaginary part of the complex dominant eigenvalue λ_{dom} is plotted versus V_i

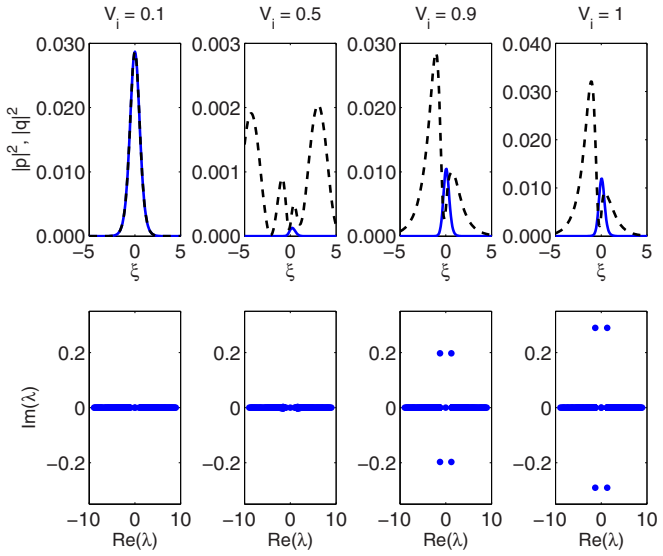

FIG. 7. (Color online) Stability spectrum for $\mu = 1.3$ and $l = 1$. Solid blue lines correspond to $|p(x)|^2$ and dashed black lines correspond to $|q(x)|^2$ for the eigenvalue λ with the maximum imaginary part, hereafter named $\lambda_{\rm dom}$. The eigenvalue spectrum is shown in the bottom row. For low V_i, the soliton is quasistable due to the smallness of $\mathrm{Im}(\lambda_{\rm dom})$, whereas for high V_i the linear perturbation modes are asymmetric and the soliton blows up.

and μ, for several l and for both the types of potentials. As is well known, solitons are stable for purely real potentials ($V_i = 0$) [34]; for low values of the imaginary part of the potential V_i a small instability arises, for all l and μ values.

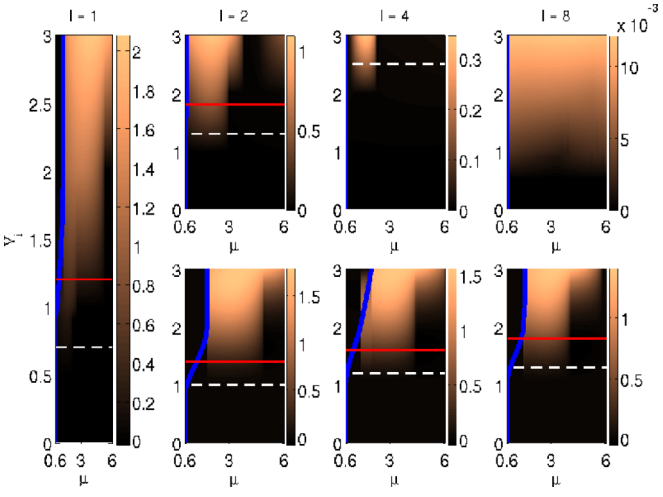

FIG. 8. (Color online) Stability eigenspectrum computed from Eq. (8) in the plane (V_i, μ): l changes as marked in the figure. Top and bottom rows depict results for potentials of type A and B, respectively. The region embedded between the two horizontal lines corresponds to the presence of complex eigenvalues in the linear spectrum, white dashed lines and red solid lines representing V_c and V_t, respectively. In general, solitons become highly unstable when $V_i > V_c$. Keeping V_i fixed, larger l enhances soliton instability for potentials of type B if compared with type A. Vertical blue lines represent the boundary between regions allowing the existence of a solitonic solution (right side) and the forbidden region (left side).

Noteworthy, solitary waves remain quasistable until the critical value of the imaginary potential is reached (the exceptional points in the linear case are indicated by the white parallel lines); i.e., $V_c \approx lV_r/2 + 1/5$ for potentials of type A, thus providing $V_c \approx 0.7$ for $l = 1$, $V_c \approx 1.2$ for $l = 2$, $V_c \approx 2.2$ for $l = 4$, and $V_c \approx 4.2$ for $l = 8$. For example, solitons are quasistable for all V_i for $l = 8$, given that the maximum considered V_i is smaller than V_c. For V_i values above the horizontal red solid lines there are no bound states for the linear potential, whereas, in the region between horizontal white dashed and red solid lines, the linear potential supports bound states subjected to amplification or decay (see also Figs. 1 and 2). For potentials of type A, stability drastically increases with l, whereas the quasistability region only slightly increases with l for potentials of type B (the region below the horizontal white dashed lines). This stability increase with l for potentials of type A can be attributed to the fact that the overlap between the soliton and the imaginary part of the potential decreases as l increases (see Fig. 3). For $V_i > V_c$, the growth factor versus the nonlinear eigenvalue μ is not monotonic: at large μ solitons become strongly localized around $\xi = 0$, thus minimizing the amount of transverse flux required from the particle conservation (see Fig. 8). This interpretation is confirmed by the behavior with l [smaller l correspond to a larger instability, i.e., greater $|\mathrm{Im}(\lambda_{\rm dom})|$] for potential of type A, and from the independence of $\mathrm{Im}(\lambda_{\rm dom})$ from l for potentials of type B. As an example, let us consider $l = 1$: when $V_i = 0.1$ the solution is quasistable for all μ values, whereas for $V_i = 1$ the instability first increases and then decreases with μ.

VI. PROPAGATION DYNAMICS

The results obtained above regarding the linear stability analysis of solitons have been checked numerically by computing soliton dynamics in the presence of noise. We employed a standard beam propagation method using a Crank-Nicolson scheme for diffraction. The Strang splitting, an asymmetric operator splitting featuring second-order accuracy, is used for simulations with high V_i, where stationary solutions are obtained near the $\mathcal{PT}$-symmetry breaking point.

We investigated field dynamics when a soliton, perturbed with Gaussian noise encompassing a magnitude 1% of the soliton amplitude, is taken as the input beam. Representative results are shown in Fig. 9. For $V_i = 0.1$ the soliton is stable over the numerical propagation length equal to $\zeta = 200$ (corresponding to about 1600 Rayleigh distances for $w_\xi \approx 0.5$), whereas for $V_i = 0.5$ the solution experiences exponential growth due to an instability mode with $\mathrm{Im}(\lambda_{\rm dom}) \approx 2 \times 10^{-3}$ (the second column in Fig. 7); noteworthy, the growth starts to be appreciable after $\zeta = 200$, in good agreement with linear stability analysis (LSA). Results from LSA are confirmed also in the presence of stronger instability: in this case field distribution loses its spatial symmetry and undergoes a much stronger exponential growth. In the bottom row of Fig. 9, transverse profiles of the beam at various longitudinal sections are shown for $V_i = 1$, for both types A and B, and for various l values. At each section the field is normalized to the local power to improve visibility. Solitons acquire an asymmetric profile across ξ while evolving, eventually converting to a strongly localized mode undergoing exponential amplification.

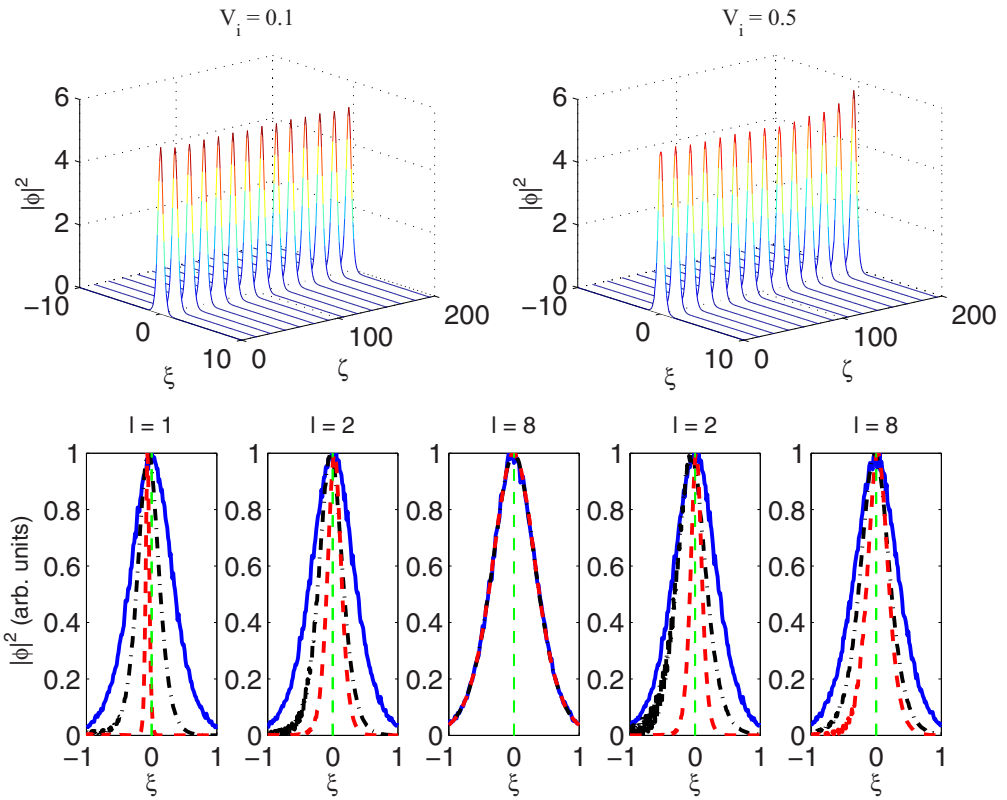

FIG. 9. (Color online) Top row: Intensity evolution of soliton solutions for $\mu = 3.4$ and (left panel) $V_i = 0.1$ showing the quasistable soliton and (right panel) $V_i = 0.5$ showing the unstable soliton. Bottom row: Transverse profiles of the solution for $V_i = 1$ and $\mu = 3.4$ for potential A are shown for $\zeta = 0$ (blue solid line), $\zeta = 100$ (black dotted line), and $\zeta = 110$ (red dashed line) for $l = 1$; $\zeta =$ [0 140 150] for $l = 2$; $\zeta =$ [0 150 200] for $l = 8$. Transverse profiles of the solution for $V_i = 1$ and $\mu = 3.4$ for potential B (last two columns) are shown for $\zeta =$ [0 130 140] for $l = 2$ and $\zeta =$ [0 129 135] for $l = 8$ showing narrowing and peak oscillation upon propagation. The profiles are normalized with power for better visibility.

The oscillations in the peak of the solution owing to OI can also be observed; the evolution along ζ of the *center of mass* of the field $\langle\xi\rangle = \int |\psi|^2 \xi d\xi / \int |\psi|^2 d\xi$ is graphed in Figs. 10 and 11, together with the width of the beam w_ξ.

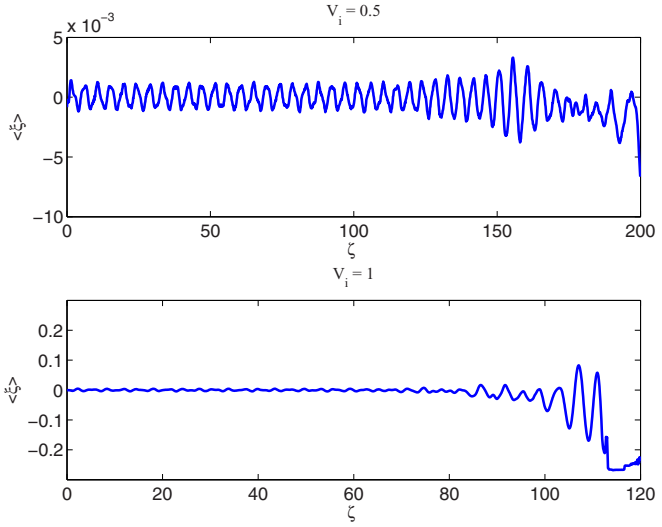

FIG. 10. (Color online) Evolution of soliton trajectory $\langle\xi\rangle$ for $V_i = 0.5$ and 1 for $l = 1$ and $\mu = 3.4$ showing the oscillations in the nonlinear wave trajectory.

Specifically, solitons with three different μ values with low, intermediate, and high magnitude were considered for the propagation studies. The intermediate value is chosen to be $\mu = 3.4$, which for low l falls in the window where the solutions are predicted to be quasistable by LSA; computed field evolutions with ζ are depicted in Fig. 11. For reference, a longitudinal distance $\zeta = 200$ corresponds to about 4000 Rayleigh distances for waves with a width of 0.3. Evolution of the beam width versus propagation distance ζ is depicted for different l values as marked for propagation both with noise (dotted lines) and without added noise (solid lines). Simulations are in very good agreement with LSA predictions: for low V_i solitons are quasistable for both the potentials; LSA predicts a small exponential amplification for $V_i = 0.5$, confirmed by numerics. A good agreement is found also for $V_i = 1$: field intensity first starts to breathe along ζ owing to the interference between the solitonic profile and the eigenmode associated with $\lambda_{\rm dom}$. At the same time, an exponential growth of the perturbative mode occurs: after a given length [the latter inversely proportional to $\mathrm{Im}(\lambda_{\rm dom})$], the perturbation becomes larger than the soliton itself, and the overall field is mainly composed by a very narrow bell-shaped wave positioned in the gain region ($\xi < 0$ in our reference system) undergoing very strong amplification supported by nonlinear self-focusing. Finally, instead of adding random noise we varied the power of the soliton conserving its transverse shape.

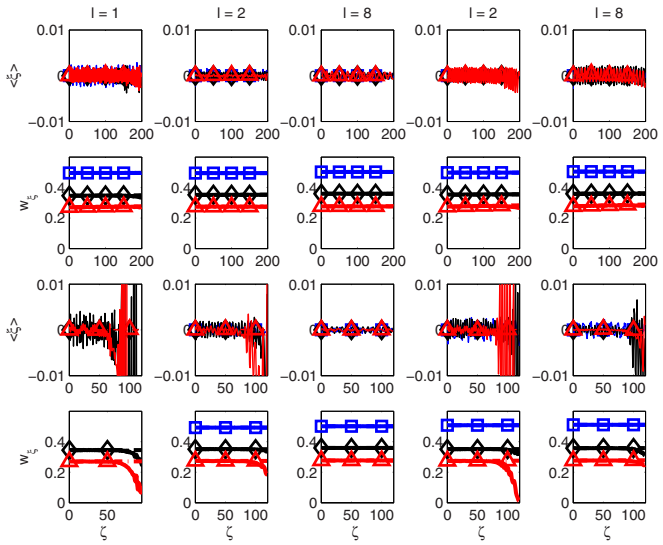

FIG. 11. (Color online) Evolution of trajectory $\langle\xi\rangle$ and width w_ξ vs ζ for $V_i = 0.5$ (top two rows) and $V_i = 1$ (bottom two rows) for potentials of type A (second and third column) and potentials of type B (last two columns) for different l as marked; for $l = 1$ both the potentials are equivalent. Dotted lines correspond to the propagation of stationary nonlinear modes, whereas solid lines correspond to wave evolution initially perturbed by 1% random noise in amplitude for $\mu = 0.7$ (□), $\mu = 3.4$ (◇), and $\mu = 6$ (△).

As depicted in the plot of beam radius in Fig. 12, solitons survive this kind of symmetric perturbation even for $V_i = 1$; in particular, solid lines represent propagation dynamics of the unperturbed soliton, whereas dashed lines represent beam evolution when the input power is increased by 1%. This

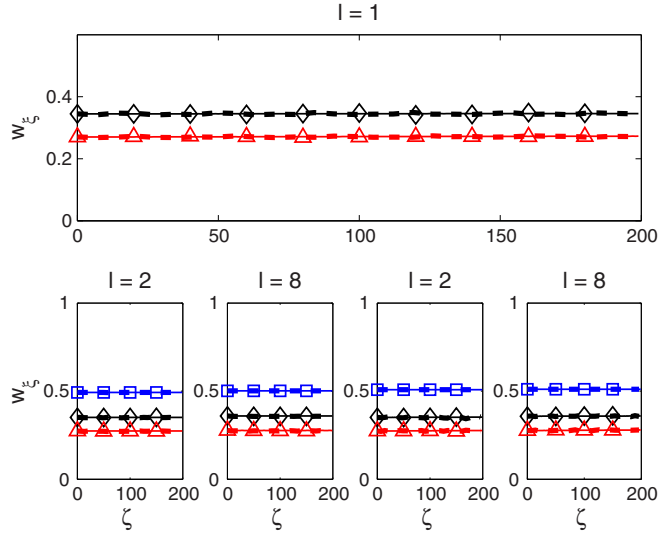

FIG. 12. (Color online) Evolution of wave radius vs ζ for $l = 1$ (first row) and potentials of type A (second row, first two columns) and potentials of type B (second row, last two columns) for different l and $V_i = 1$; for $l = 1$ both the potentials are equivalent. Solid lines correspond to the propagation of unperturbed solitons, whereas dashed lines correspond to evolution with 1.01 of the soliton power for $\mu = 0.7$ (□), $\mu = 3.4$ (◇), and $\mu = 6$ (△).

behavior demonstrates once again that the main mechanism for the insurgence of instability is related with $\mathcal{PT}$-symmetry breaking: in fact, a symmetric perturbation does not yield any exponential growth of the field, given that the parity of the system is conserved by this kind of perturbation. Physically, instability is strictly related to the presence of some linear eigenstates encompassing a complex eigenvalue, a general property of localized complex potentials, different to what happens in periodic systems [8,9]. Thus, we can conclude that $\mathcal{PT}$-symmetric solitons supported by localized potentials are in general unstable, irrespective of the profile of the refractive index. The instability manifests appreciably at large propagation distances with respect to the Rayleigh length for $V_i < V_c$, whereas solitons survive for short distances when $V_i \geqslant V_c$. For example, in Ref. [8] authors claim solitons are stable, whereas we demonstrate numerically (results not shown here) that solitons in Scarff II potentials are actually subjected to a small exponential growth, an important detail in applications such as laser cavities.

VII. CONCLUSIONS

We studied the existence and stability of $\mathcal{PT}$-symmetric solitons in a medium with Kerr nonlinearity into which a linear localized $\mathcal{PT}$-symmetric defect is embedded. Effects of the transverse profile of gain or loss on the existence of solitons are studied by considering two different kinds of localized photonic potentials differing in their imaginary part. The real part of the potential is assumed to be super-Gaussian, whereas the imaginary part is varied: in one case the imaginary part is equal to the first derivative of the real part, whereas in the other case the imaginary part is taken similar to a Hermitian super-Gaussian function of order 1, regardless of the shape of the real part of the photonic potential. The imaginary part of the potential strongly affects the field dynamics, thus allowing the control of wave evolution acting on the gain or loss profiles solely. Soliton profiles are found to depend strongly on the imaginary potential, undergoing lateral reshaping in order to compensate transverse flux of energy occurring from the gain towards the loss region. Solitons preserving their shape and amplitude in propagation are found to exist even when the ground eigenstates in the linear regime feature a complex spectrum; that is, nonlinearity is able to reestablish the $\mathcal{PT}$ symmetry, broken in the absence of the Kerr effect. Interestingly, when transverse flux of energy occurs (i.e., in the presence of dissipative effects), a power threshold for the soliton existence appears: we discussed how this threshold depends on the linear potential, both the real and the imaginary part. We then discussed soliton reaction to small perturbations using linear stability analysis. In general we found that solitons become strongly unstable when the underlying linear system is beyond the exceptional point, showing dominant perturbative modes localized into the gain region, thus breaking the parity of the wave distribution, and with a growth factor increasing with the magnitude of the gain. In contrast with available literature [8,32], a much smaller instability is found even below the exceptional point, resulting in an exponential amplification negligible over several Rayleigh distances. We checked our findings via BPM simulations, showing that unstable solitons undergo

oscillatory instability when perturbed with a parity-breaking noise, eventually resulting in exponentially growing modes localized into the gain region. Conversely, solitons survive when their initial spatial symmetry is conserved by the applied perturbation, thus confirming that $\mathcal{PT}$-breaking mechanisms are responsible for the observed wave instabilities.

We believe that our results can find application in the design of a novel kind of semiconductor laser presenting exotic and novel properties [7,41], where the transverse light confinement is ensured by means of a linear waveguide and inhomogeneous gain or loss can be achieved by space-dependent charge injection, something realizable with current technology, for example, in AlGaAs systems: we expect that the Kerr effect plays a fundamental role in these setups owing to the high intensities associated with cavities, permitting also new functionalities such as the switching between different emission states as the gain of the system is varied.

ACKNOWLEDGMENTS

J.C.P. gratefully acknowledges Fundação para a Ciência e a Tecnologia (FCT) Grant No. SFRH/BPD/77524/2011. L.D. acknowledges University Grants Commission (UGC) Research Fellowship in Science for Meritorious Students (RFSMS) Grant for financial support. V.C.K. acknowledges the Associateship of Inter-University Centre for Astronomy and Astrophysics (IUCAA), Pune.

[1] C. M. Bender and S. Boettcher, Phys. Rev. Lett. **80**, 5243 (1998).
[2] C. M. Bender, D. C. Brody, and H. F. Jones, Phys. Rev. Lett. **89**, 270401 (2002).
[3] C. M. Bender, S. Boettcher, and P. N. Meisinger, J. Math. Phys. **40**, 2201 (1999).
[4] C. M. Bender, D. C. Brody, H. F. Jones, and B. K. Meister, Phys. Rev. Lett. **98**, 040403 (2007).
[5] Y.-C. Lee, M.-H. Hsieh, S. T. Flammia, and R.-K. Lee, Phys. Rev. Lett. **112**, 130404 (2014).
[6] C. E. Rüter, K. G. Makris, R. El-Ganainy, D. N. Christodoulides, M. Segev, and D. Kip, Nat. Phys. **6**, 192 (2010).
[7] Y. D. Chong, L. Ge, and A. D. Stone, Phys. Rev. Lett. **106**, 093902 (2011).
[8] Z. H. Musslimani, K. G. Makris, R. El-Ganainy, and D. N. Christodoulides, Phys. Rev. Lett. **100**, 030402 (2008).
[9] Y. Lumer, Y. Plotnik, M. C. Rechtsman, and M. Segev, Phys. Rev. Lett. **111**, 263901 (2013).
[10] N. Bender, S. Factor, J. D. Bodyfelt, H. Ramezani, D. N. Christodoulides, F. M. Ellis, and T. Kottos, Phys. Rev. Lett. **110**, 234101 (2013).
[11] A. Mostafazadeh, J. Math. Phys. **43**, 205 (2002).
[12] R. El-Ganainy, K. G. Makris, D. N. Christodoulides, and Z. H. Musslimani, Opt. Lett. **32**, 2632 (2007).
[13] S. Klaiman, U. Günther, and N. Moiseyev, Phys. Rev. Lett. **101**, 080402 (2008).
[14] A. Guo, G. J. Salamo, D. Duchesne, R. Morandotti, M. Volatier-Ravat, V. Aimez, G. A. Siviloglou, and D. N. Christodoulides, Phys. Rev. Lett. **103**, 093902 (2009).
[15] L. Feng, M. Ayache, J. Huang, Y.-L. Xu, M.-H. Lu, Y.-F. Chen, Y. Fainman, and A. Scherer, Science **333**, 729 (2011).
[16] L. Feng, Y.-L. Xu, W. S. Fegadolli, M.-H. Lu, J. E. B. Oliveira, V. R. Almeida, Y.-F. Chen, and A. Scherer, Nature Materials **12**, 108 (2012).
[17] A. Regensburger, C. Bersch, M.-A. Miri, G. Onishchukov, D. N. Christodoulides, and U. Peschel, Nature (London) **488**, 167 (2012).
[18] T. Eichelkraut, R. Heilmann, S. Weimann, S. Stutzer, F. Dreisow, D. N. Christodoulides, S. Nolte, and A. Szameit, Nat. Commun. **4**, 2533 (2013).
[19] Z. Lin, H. Ramezani, T. Eichelkraut, T. Kottos, H. Cao, and D. N. Christodoulides, Phys. Rev. Lett. **106**, 213901 (2011).
[20] K. G. Makris, R. El-Ganainy, D. N. Christodoulides, and Z. H. Musslimani, Phys. Rev. Lett. **100**, 103904 (2008); Phys. Rev. A **81**, 063807 (2010); Int. J. Theor. Phys. **50**, 1019 (2011).
[21] S. Longhi, Phys. Rev. Lett. **103**, 123601 (2009).
[22] S. Longhi, Phys. Rev. A **82**, 031801 (2010).
[23] A. E. Miroshnichenko, B. A. Malomed, and Y. S. Kivshar, Phys. Rev. A **84**, 012123 (2011).
[24] B. Peng, Ş. K. Özdemir, F. Lei, F. Monifi, M. Gianfreda, G. L. Long, S. Fan, F. Nori, C. M. Bender, and L. Yang, Nature Physics **10**, 394 (2014).
[25] G. I. Stegeman and M. Segev, Science **286**, 1518 (1999).
[26] J. Zeng and Y. Lan, Phys. Rev. E **85**, 047601 (2012).
[27] S. Nixon, L. Ge, and J. Yang, Phys. Rev. A **85**, 023822 (2012).
[28] H. Li, X. Jiang, X. Zhu, and Z. Shi, Phys. Rev. A **86**, 023840 (2012).
[29] C. P. Jisha, A. Alberucci, V. A. Brazhnyi, and G. Assanto, Phys. Rev. A **89**, 013812 (2014).
[30] H. Wang and J. Wang, Opt. Express **19**, 4030 (2011).
[31] N. V. Alexeeva, I. V. Barashenkov, A. A. Sukhorukov, and Y. S. Kivshar, Phys. Rev. A **85**, 063837 (2012).
[32] S. Hu, X. Ma, D. Lu, Z. Yang, Y. Zheng, and W. Hu, Phys. Rev. A **84**, 043818 (2011).
[33] Z. Shi, X. Jiang, X. Zhu, and H. Li, Phys. Rev. A **84**, 053855 (2011).
[34] Y. S. Kivshar and G. P. Agrawal, *Optical Solitons* (Academic, San Diego, 2003).
[35] C. P. Jisha, A. Alberucci, R.-K. Lee, and G. Assanto, Optics Express **21**, 18646 (2013).
[36] L. P. Pitaevskii and S. Stringari, *Bose-Einstein Condensation* (Oxford University, New York, 2003).
[37] Z. Ahmed, Phys. Lett. **282**, 343 (2001).
[38] L. N. Trefethen, *Spectral Methods in MATLAB* (SIAM, Philadelphia, 2000).
[39] S. M. Jensen, IEEE J. Quantum Electron. **18**, 1580 (1982).
[40] I. V. Barashenkov, D. E. Pelinovsky, and E. V. Zemlyanaya, Phys. Rev. Lett. **80**, 5117 (1998).
[41] L. Feng, Z. J. Wong, R. Ma, Y. Wang, and X. Zhang, arXiv:1405.2863 (2014).